



Cyclic deformation behaviour, microstructural evolution and fatigue life of duplex steel AISI 329 LN



H. Knobbe^a, P. Starke^{b,c,*}, S. Hereñú^d, H.-J. Christ^a, D. Eifler^b

^a Institut für Werkstofftechnik, Universität Siegen, Germany

^b Lehrstuhl für Werkstoffkunde, Technische Universität Kaiserslautern, Germany

^c Lehrstuhl für Zerstörungsfreie Prüfung und Qualitätssicherung, Universität des Saarlandes, Germany

^d Instituto de Física Rosario, CONICET-UNR, Av. 27 de Febrero 210 Bis, 2000 Rosario, Argentina

ARTICLE INFO

Article history:

Received 23 January 2015

Received in revised form 30 April 2015

Accepted 10 May 2015

Available online 23 May 2015

Keywords:

Duplex steel

Fatigue life calculation

PHYBAL

Microstructure

Transmission electron microscopy

ABSTRACT

This paper summarises fatigue results obtained on the duplex steel AISI 329 LN (German designation 1.4462). For the characterisation of the fatigue behaviour, the mechanical stress–strain hysteresis loops, the temperature change and the evolution of the electrical resistance were monitored. Transmission electron microscopy was performed to investigate the microstructural changes caused by the fatigue loading. The data were used to apply the fatigue life calculation method “PHYBAL_{LT}”. This procedure requires only one load increase test and two constant amplitude tests for a timesaving and material-efficient assessment of *S*–*N* (Woehler) curves. The method has already been successfully applied to different carbon and austenitic steels as well as lightweight materials. The results show an excellent agreement between the conventionally determined and the calculated fatigue lifetimes. This agreement is rationalized on a microstructural basis.

© 2015 Elsevier Ltd. All rights reserved.

1. Introduction

The characterisation of changes in the microstructure due to cyclic loading is of major importance for the understanding of the fatigue mechanisms and are the basis for an improvement of fatigue life assessment concepts in particular for complex metallic materials. Hence, the knowledge on the microstructure evolution is fundamental for a robust and unerring fatigue-resistant design as well as an optimised material selection ensuring safe and economic operation conditions of metallic components, particularly under the aspect of lightweight construction. Generally, mechanical stress–strain hysteresis loop measurements are performed to describe the macroscopic response of materials to mechanical cyclic loading. If accessible, the plastic strain amplitude is preferred to characterise the degree of fatigue damage per loading cycle [1,2]. However, various experimental techniques are available to determine cyclic stress–strain curves of metallic materials [1]. In recent years, it has become more and more common to supplement the acquisition of fatigue data by additional thermal [3–8] and electrical [9–13] measurements. The application of thermographic methods on cyclically loaded steel specimens is reported for instance in

[4], the determination of the fatigue limit on the basis of energy dissipation is described in [7]. Apart from the geometry, the electrical resistance depends on the resistivity, which is strongly influenced by microstructural changes which are often combined with cyclic softening and/or hardening processes. Investigations of cyclically deformed copper reveal a systematic increase of resistivity with increasing dislocation density [9].

The scope of this work is focused on the characterisation of the cyclic deformation behaviour in the “high cycle fatigue” (HCF) and “very high cycle fatigue” (VHCF) regime up to 10^8 cycles as well as the application of the physically-based fatigue life calculation method “PHYBAL_{LT}” in the HCF regime of duplex steel AISI 329 LN. It is known that VHCF regime crack initiation can be shifted from the surface to defects such as inclusions and pores or to non-defect sites in the interior of the material [14]. Non-defect sites mean local inhomogeneities leading to stress or plastic strain concentrations such as phase boundaries between cementite and ferrite, a particularly large grain or grain arrangements favorably oriented for slip, where no pre-existing defect is present. In this study, the transition from surface to subsurface crack initiation is not considered in the lifetime calculation since only in two cases large non-metallic inclusions were observed initiating subsurface crack formation. Thus, the lifetime calculation is only applied to the HCF regime.

* Corresponding author at: Lehrstuhl für Zerstörungsfreie Prüfung und Qualitätssicherung, Universität des Saarlandes, Germany.

E-mail address: peter.starke@uni-saarland.de (P. Starke).

2. Material

Austenitic–ferritic steels typically consist of a strong phase (in most cases the α ferrite) and a soft phase (mostly the γ austenite) leading to a beneficial combination of mechanical properties such as relatively high strength and ductility in combination with superior corrosion resistance due to the high chromium content. Thus, duplex steels are often used for automotive, oil, petrochemical and off-shore applications. The material investigated in this study is the austenitic–ferritic duplex stainless steel AISI 329 LN (German designation 1.4462). The chemical composition is given in Table 1. The test specimen blanks were heat-treated in laboratory air at 1250 °C for 4 h resulting in a homogeneous microstructure consisting of nearly 100% ferrite. This process step was followed by controlled cooling down to 1050 °C in 3 h leading to the precipitation of the austenitic phase as shown in the iron–chromium–nickel phase diagram (Fig. 1). Finally, the material was water-quenched to prevent the formation of the brittle σ phase. After heat treatment the surface oxide layer was mechanically removed. The machined specimens were ground followed by electropolishing of the gauge length, resulting in a very smooth surface with an average roughness of $R_a < 0.2 \mu\text{m}$. The resulting microstructure (Fig. 2) consists of a ferritic matrix (dark areas) with austenitic islands (bright areas) and a nearly equal ferrite (54 area-%) and austenite (46 area-%) volume fraction as seen in the phase representation obtained on a cross section by means of electron back-scattered diffraction. The average grain sizes are 33 μm and 46 μm for ferrite and austenite, respectively. The micro hardness HV0.05 was measured separately for each phase and values of 260 and 220 were obtained for α and γ , respectively. The alloying elements significantly affect the local mechanical properties of the phases. For example, nitrogen additions increase the hardness of the austenitic phase whereas chromium and molybdenum promotes higher hardness of the ferritic phase [15–17]. However, ferrite remains the harder phase in the material investigated, and this determines the mechanism of fatigue damage initiation, i.e., the crack formation site.

Table 2 summarises the strength parameters of the material after the heat treatment determined in a tensile test.

The microstructure of the material was examined in a Philips EM 300 transmission electron microscope (TEM) operating at 100 kV. These investigations were aimed at a characterisation of microstructural changes such as the evolution of the dislocation arrangement and density as a function of loading amplitude, in order to provide a sound basis for the evaluation of the applicability of the life assessment method PHYBAL_{LIT}.

3. Test setup

Load increase tests (LITs) and constant amplitude tests (CATs) were carried out at a stress ratio of $R = -1$ with servohydraulic and resonant testing systems at frequencies of $f = 5$ (LIT, CAT), 15 (CAT), 130 (LIT, CAT) and 300 Hz (CAT) at ambient temperature. The LITs at 5 Hz were performed with a continuous increase of the stress amplitude, whereas at 130 Hz the stress amplitude was increased in a stepwise manner. The procedure of the continuous LIT is schematically represented in Fig. 3.

The LITs and CATs with a frequency of 5 Hz were carried out using a triangular load command signal on a 100 kN

servohydraulic testing system (Schenck) at the University of Kaiserslautern. For CATs with frequencies > 5 Hz a 250 kN resonant testing machine (Rumul, resonant testing frequency 130 Hz) and a

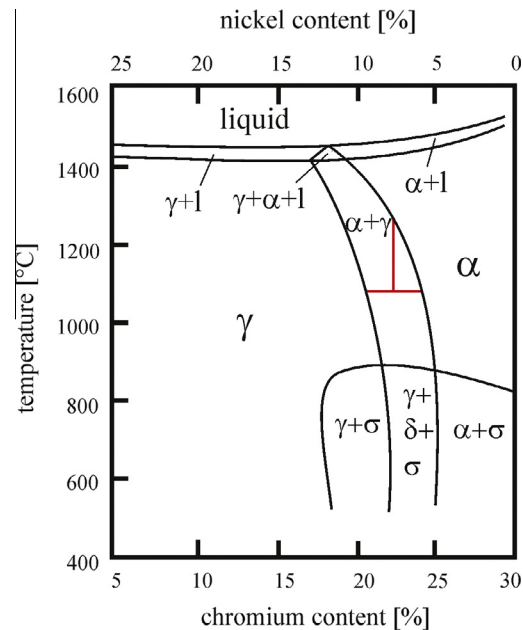


Fig. 1. Iron–chromium–nickel phase diagram for an iron content of 70 wt.%.

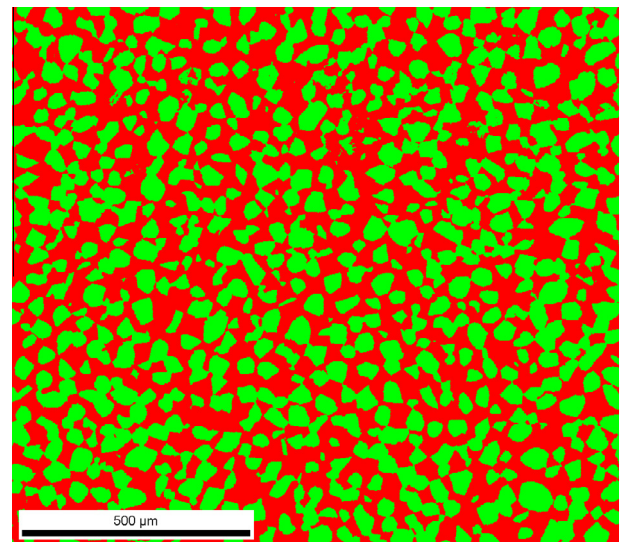


Fig. 2. Microstructure of duplex stainless steel AISI 329 LN after heat treatment obtained by electron back-scattered diffraction contrast used for phase identification.

Table 2
Mechanical properties of duplex stainless steel AISI 329 LN.

Modulus (GPa)	R_{UTS} (MPa)	R_{YS} 0.1 (MPa)	R_{YS} 0.2 (MPa)	A (%)
200	707	381	445	36

Table 1
Chemical composition of duplex stainless steel AISI 329 LN in wt.%.

Fe	Cr	Ni	Mo	Mn	Si	P	S	Cu	Ti	Co	N	C
Bal.	21.91	5.58	3.08	1.83	0.53	0.023	0.002	0.11	0.03	0.07	0.19	0.02

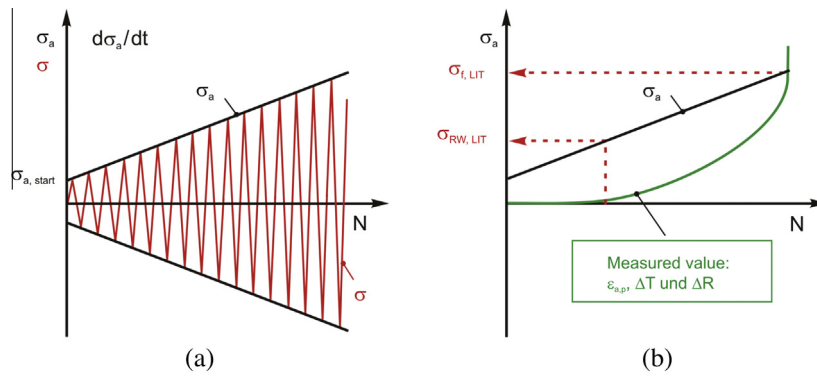


Fig. 3. Stress amplitude σ_a (a) and plastic strain amplitude $\epsilon_{a,p}$, change in temperature ΔR and electrical resistance ΔR (b) as well as the estimated endurance limit $\sigma_{RW,LIT}$ and the stress amplitude resulting in failure $\sigma_{f,LIT}$ in a continuous load increase test (schematic representation).

1000 Hz high frequency servohydraulic testing system (MTS, testing frequencies 15 Hz and 300 Hz) at the University of Siegen were used. The change from a triangular to a sinusoidal waveform is caused by the actuating principles of the testing systems using an electro-magnetic drive and a voice-coil valve controlled hydraulic cylinder, respectively. Compressed air with 8 bar was used to keep the specimen temperature below 50 °C also in the tests with a frequency of 130 and 300 Hz. This procedure is necessary because of the high energy dissipation in the duplex steel. The three specific geometries of the unnotched fatigue specimens (Fig. 4) are related to the requirements of the testing systems due to their actuating drives and specific clamping devices which e.g. in case of the 130 Hz resonant testing system (Fig. 4a) requires a notch in the gripping section of the specimen. The tests at 300 Hz were discontinued at the ultimate number of cycles of $1 \cdot 10^8$, the tests at 130 Hz at $5 \cdot 10^7$ cycles and those with 5 and 15 Hz were truncated at $2 \cdot 10^6$ cycles, if failure has not occurred earlier. The ultimate numbers of cycles were defined on the basis of the respective test frequencies and the resulting experimental duration. A detailed overview of the experiment plan is given in Table 3.

In order to characterise the cyclic deformation behaviour, stress–strain hysteresis loops (only at 5 Hz), the change in temperature (for all frequencies of 5, 15, 130 und 300 Hz) and the electrical resistance (only at 5 Hz) were monitored. In the case of the resonant system the change in frequency can be used as additional information. For the measurement of the strain at a frequency of 5 Hz, a conventional extensometer with a measuring length of 10 mm was fixed in the middle of the gauge length. The change in temperature ΔT was measured with one thermocouple in the middle of the gauge length (T_1) and two thermocouples (T_2 and

Table 3
Experiment plan.

Specimen geometry	Frequency (Hz)	Load signal	Number of cycles	Machine type	Type of experiment
Fig. 4a	130	Sinusoidal	Until failure or $5 \cdot 10^7$	Rumul	CAT
Fig. 4a	130	Sinusoidal, increase stepwise	Until failure	Rumul	LIT
Fig. 4b	300	Sinusoidal	Until failure or $1 \cdot 10^8$	MTS	CAT
Fig. 4b	15	Sinusoidal	Until failure or $2 \cdot 10^6$	MTS	CAT
Fig. 4c	5	Triangular	Until failure	Schenck	CAT
Fig. 4c	5	Triangular, continuous increase	Until failure	Schenck	LIT

T_3) at the elastically loaded gripping section of the specimens. For electrical resistance measurements a DC-power supply was attached to both specimen shafts and ΔR was measured with two wires spot welded at the transition of the gauge length and the shafts (Fig. 5), cf. [18,19].

4. Results and discussion

4.1. Load increase tests

LITs have proven to allow for a fast first assessment of the endurance limit using just one single specimen [18,19]. It must be noted that this statement only holds true, if the term endurance limit relates to a commonly used ultimate number of cycles in the HCF regime, e.g., $N_{max} = 2 \cdot 10^6$ cycles. In the LITs of this study, the courses of the quantities monitored ($\Delta \epsilon$, ΔT and ΔR) can be exploited to characterise the cyclic stress–strain response and can also be used as data base for the fatigue life calculation “PHYBAL_{LIT}”. The absolute values of the measured quantities in the LITs depend, among others, on the test frequency which is linked to the dissipated energy per time sequence as well as to the change in dislocation movements in the volume plastically deformed. The final part of a LIT is exemplarily shown in Fig. 6 starting at $80 \cdot 10^3$ cycles. The test started at a stress amplitude σ_a of 100 MPa and was performed at a stress amplitude increase rate of $10.7 \cdot 10^{-3}$ MPa/s. $\sigma_{a,start}$ is usually selected in the range of

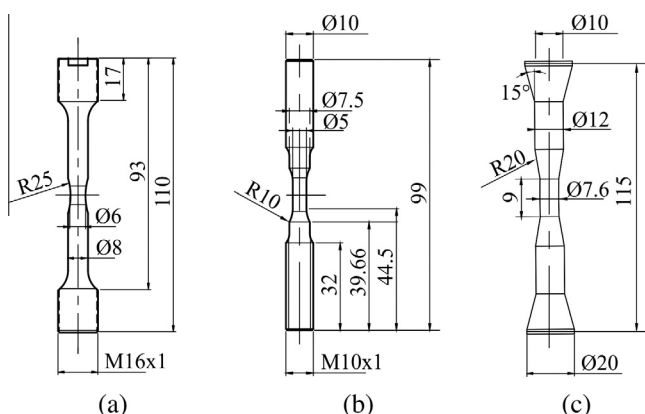


Fig. 4. Specimen geometries for the different testing facilities, (a) resonant testing system (130 Hz), (b) servohydraulic testing system (15 Hz and 300 Hz) and (c) servohydraulic testing system (“PHYBAL” tests at 5 Hz).

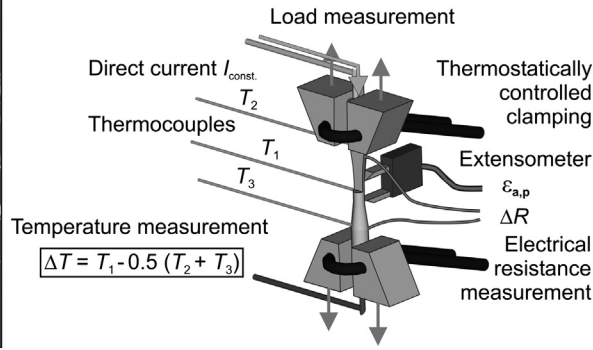
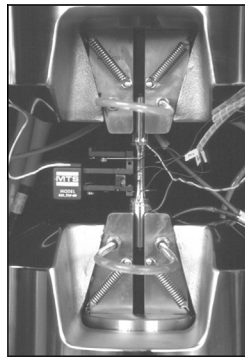
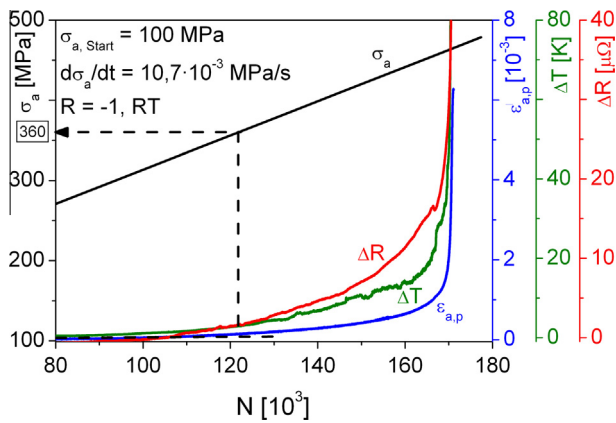
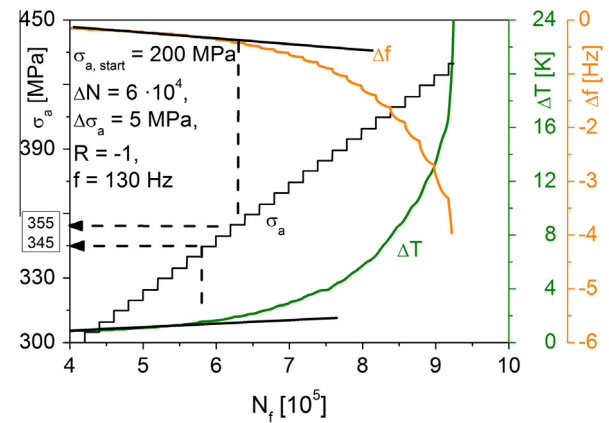


Fig. 5. Experimental setup.

Fig. 6. Stress amplitude σ_a , plastic strain amplitude $\varepsilon_{a,p}$, change in temperature ΔT and electrical resistance ΔR in a continuous load increase test at a frequency of 5 Hz.Fig. 7. Change in temperature ΔT and change in frequency Δf in a stepwise load increase test at a frequency of 130 Hz (resonant testing system).

20–40% of the yield strength in order to avoid any plastic deformations in the first cycles of the test. The plastic strain amplitude $\varepsilon_{a,p}$, the change in temperature ΔT and the change in electrical resistance ΔR are plotted versus the number of cycles N . The initial materials response at lower stress amplitudes is characterised by an approximately linear increase. A significant change in the slope of the $\varepsilon_{a,p}$ - N , ΔT - N and ΔR - N curve of the LIT occurs at $\sigma_{RW,LIT} = 360$ MPa ($\sigma_{RW,LIT}$: endurance limit estimated in the LIT) and is related to first plastic deformations in the gauge length. The change in the slope at a stress amplitude $\sigma_{RW,LIT}$ is caused by increasing plastic deformations and can be used for the assessment of the endurance limit [3,18,19]. The stress amplitude $\sigma_{f,LIT} = 478$ MPa led to specimen failure in this experiment. Both values $\sigma_{RW,LIT} = 360$ MPa and $\sigma_{f,LIT} = 478$ MPa are of major importance for setting the stress amplitudes of the CATs required for the fatigue life prediction according to “PHYBAL_{LIT}”.

Additional LITs were performed at a frequency of 130 Hz to underline the adaptability of the “PHYBAL_{LIT}”-concept to high frequency conditions. Fig. 7 shows the materials response to a LIT with a stepwise increase of σ_a in terms of the change in temperature ΔT and the change in resonant testing frequency Δf . The starting stress amplitude was set at 200 MPa and increased in steps of $\Delta\sigma_a = 5$ MPa. The specimen was cyclically loaded for $N = 6 \cdot 10^4$ cycles at each stress amplitude.

The testing frequency of a resonator is a function of the specimen geometry and the stiffness of the specimen, which is directly related to the change in microstructure during cycling loading. Consequently, cyclic softening due to dislocation reactions and in advanced fatigue states also crack propagation processes in the LIT result in a total frequency drop of 4 Hz close to fracture. The

discontinuous course of the frequency as well as the change in temperature can be explained by stepwise increased stress amplitudes and transient response effects of the resonator system within the LIT. Similar to the continuous LIT at 5 Hz the endurance limit can be assessed by the point of deviation from linear change of temperature and frequency giving $\sigma_{RW,LIT} = 345$ and 355 MPa, respectively.

4.2. Constant amplitude tests

Constant amplitude tests were performed on servohydraulic and resonant testing systems with frequencies of 5, 15, 130 and 300 Hz. It is to be noted that the results of the CATs were not statistically validated within this investigation. It has to be noted that the results of the CATs were not statistically validated within this investigation. The stress amplitude vs. fatigue life according to Woehler is given in Fig. 8. Different symbols allow for the differentiation with respect to testing frequency, load signal, specimen geometry and type of failure. Scatter effects with respect to the number of cycles to failure are mainly influenced by the microstructure of the material and not by testing frequency. Failures caused by inclusions occur only at lifetimes above $2 \cdot 10^7$ cycles. Data points marked with an arrow indicate run-outs, while the numeric next to some run-outs indicate the number of specimens tested under the same conditions. An evaluation of these data in accordance to the staircase method led to a fatigue strength of $\sigma_a = 382$ MPa for a maximum number of 10^8 cycles.

4.3. TEM investigations

Transmission electron microscopy was performed in the initial condition and after fatigue testing in order to characterise changes

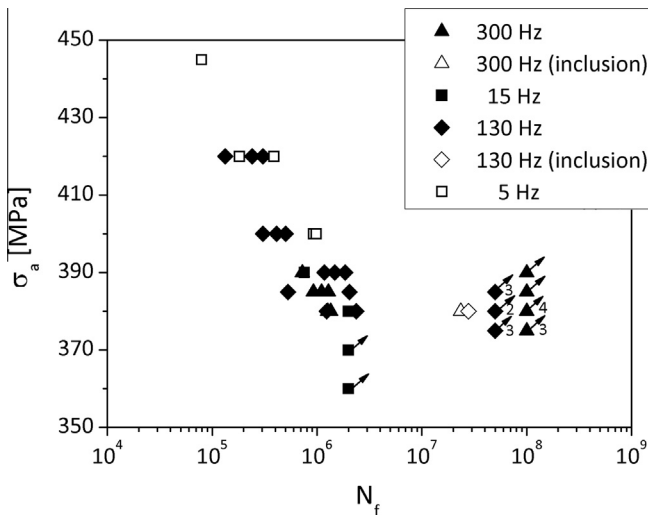


Fig. 8. Stress amplitude–lifetime relation (S–N curve) for different test frequencies.

in the microstructure, especially in the dislocation arrangement resulting from cyclic loading. Fig. 9 shows TEM micrographs of both phases, ferrite and austenite, in the condition after heat treatment prior to testing. The ferritic microstructure is characterised by a low dislocation density and small precipitates dispersed in the matrix (Fig. 9a). This is also documented by the superlattice reflections appearing in the diffraction pattern (for instance, the one marked by the white circle in Fig. 9a). As clearly visible in the bright field image, the needle-like precipitates are well aligned along low-order crystal planes of the ferrite in an intragranular manner. It is very likely that these particles are Cr_2N precipitates formed as a result of the heat treatment, in particular during the fast cooling by water quenching from 1050 °C to room temperature. Supersaturation of the ferrite and quenched-in nitrides are the consequences if fast cooling from a high solution temperature is performed [20]. On the contrary intergranular equilibrium type precipitates typically occur during ageing between 700–900 °C, decorating the α/α grain or α/γ phase boundaries [21]. On the other hand, no evidences of nitrogen precipitates were found in case of the austenite mainly because the nitrogen solubility is much higher in fcc austenite than in bcc ferrite (Fig. 9b). Here, more dislocations are visible aligned in a planar manner (marked by the arrow). The occurrence of dislocations may be a result of the fast cooling procedure as well, while the dislocation arrangement is probably due to the nitrogen addition. It is well known that nitrogen changes the slip character of austenite from wavy to planar [22].

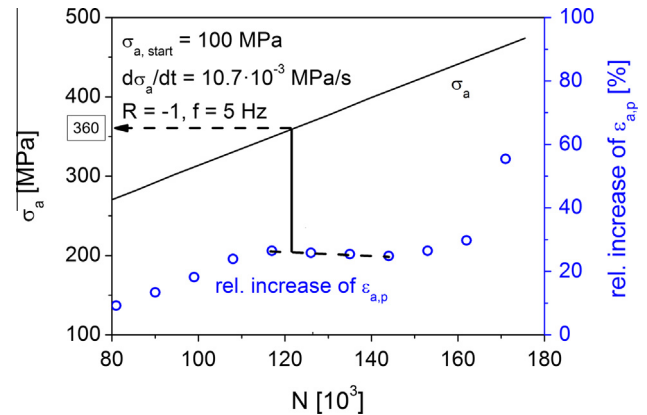


Fig. 10. Stress amplitude and relative increase of the plastic strain amplitude in a continuous load increase test performed at a frequency of 5 Hz.

Fig. 10 again shows data from the continuous LIT (compare Fig. 6) carried out at a frequency of 5 Hz. Average values of the plastic strain amplitude were determined for every $9 \cdot 10^3$ cycles and the relative plastic strain amplitude is defined as the relation of two successive average values of $\varepsilon_{a,p}$. In Fig. 10 besides the continuously increasing stress amplitude the relative increase of the plastic strain amplitude is plotted vs. the number of cycles N in comparison to the slope of the absolute values of the plastic strain amplitude shown in Fig. 6. The representation of the relative plastic strain amplitude illustrates that the cyclic deformation behaviour is a result of the individual deformation behaviour of the austenitic and ferritic phase of the investigated duplex steel. The first change in the slope of the relative increase of the plastic strain amplitude at $\sigma_a = 360$ MPa is dominated by cyclic hardening processes of the austenitic phase. For stress amplitudes slightly above $\sigma_{\text{RW,LIT}}$ besides cyclic softening of the ferritic phase first cyclic hardening processes of the austenite appear. The superimposition of cyclic softening and hardening processes results in an inflection of the slope of the relative increase of the plastic strain amplitude which is followed by a nearly horizontal section. Then again for $\sigma_a > 400$ MPa cyclic softening of the ferritic phase dominates the material behaviour with continuous cyclic softening up to crack initiation.

The values of $\sigma_a = 360$ and 400 MPa are determined by the deviation from the linear course of 3 consecutive points with an accuracy deviation of $R^2 < 0.8$.

In order to correlate this cyclic deformation behaviour with the microstructure the specimens of two load increase tests, which were finished at 300 MPa and 380 MPa, were chosen for the

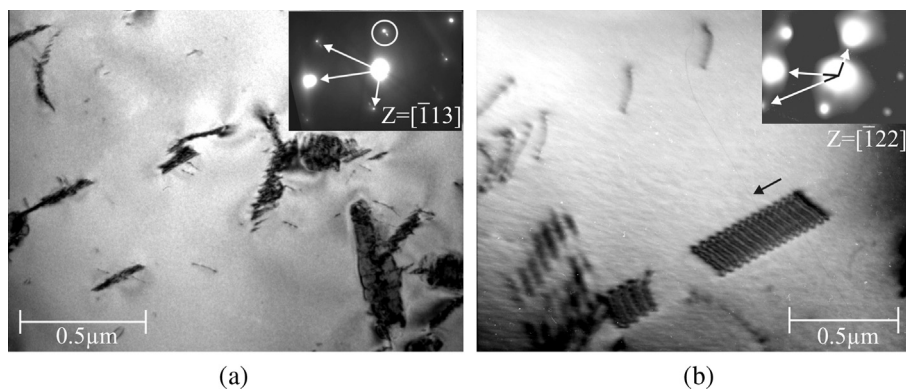


Fig. 9. TEM micrographs of the duplex steel after heat treatment showing the ferritic phase (a) and the austenitic phase (b).

preparation of TEM samples. Fig. 11 shows TEM micrographs of the ferritic phase from the load-increase test finished at 300 MPa.

In Fig. 11a, the needle-like Cr_2N precipitates, which were already shown in Fig. 9a, are visible, but again no dislocations are appreciable. Fig. 11b shows another grain with the same kind of needles together with some dislocations. However, the density of these few dislocations is very low, and it is likely that they are not a result of the cyclic loading, but have been in the material before. The arrangement is very planar, which is rather unlikely for bcc alloys after cyclic plastic deformation [23]. Thus, ferrite remains inactive during cyclic loading at low stress amplitudes.

On the contrary, a cyclically induced dislocation formation was found in the austenite. As Fig. 12a shows, a planar structure with a higher dislocation density prevails. At least two slip systems are activated as a result of cyclic plastic deformation. Fig. 12b shows a phase boundary separating austenite (left part) from ferrite (right part). Dislocations, which belong to different slip systems, pile up against the phase boundary in the austenite, whereas no dislocations were found in the ferrite. These results show that at low stress amplitudes the ferrite does not contribute to plastic deformation because of its higher yield strength as compared to austenite. Although austenite is plastically deformed, the obviously strong barrier effect of the phase boundaries prevents the dislocations from overcoming these obstacles. The observed “true” fatigue limit of the material can be attributed to this barrier effect which probably holds true not only regarding the dislocation motion but also with respect to the propagation behaviour of microstructurally small cracks.

TEM investigation of specimens fatigued at a high stress amplitude of 380 MPa, which is close to the value of the conventionally observed fatigue limit, show a high dislocation density in ferritic

grains as well (Fig. 13). Almost no Cr_2N precipitates are appreciable in the grain shown in Fig. 13a and the dislocations are distributed very homogeneously. Since the dislocation lines are intersecting, slip must have taken place on more than one slip system.

The grain shown in Fig. 13b contains some Cr_2N particles interacting with the dislocations. Some dislocation lines are bowed, but most of the dislocations appear as straight lines. This observation suggests that nitrides might have an effect on the strength of ferrite grains by blocking dislocation movement. However, since the distribution of quenched-in nitrides is rather inhomogeneous, it is unlikely to reflect this effect in the macroscopic measurements.

Fig. 14 shows the austenitic phase and a phase boundary in the same specimen. Again, a planar dislocation distribution with two activated slip systems is present, but with a higher density as compared to the specimen fatigued at a lower stress amplitude (compare Fig. 14a with Fig. 12a). Fig. 14b shows an α/γ -phase boundary with dislocations in both grains. In one case, the dislocations seem to have crossed the boundary and slightly changed their moving direction. As dislocations are able to overcome the barrier of the phase boundary, a crack initiated at such a location can possibly grow and lead to final failure. The failure of some specimens from CATs performed at 380 MPa confirms this assumption.

At higher stresses, obviously both phases contribute to the plastic deformation of the material. This change in deformation mechanism is also noticeable when looking at the resistivity and temperature plots in Fig. 6. The change in the slope is obviously directly correlated with the microstructural changes. Non-linear behaviour starts with the beginning of ferrite activity, since both major phases of the material are then involved in plastic deformation. This leads to higher dislocation densities and thus higher increase of resistivity, relative temperature and plastic strain.

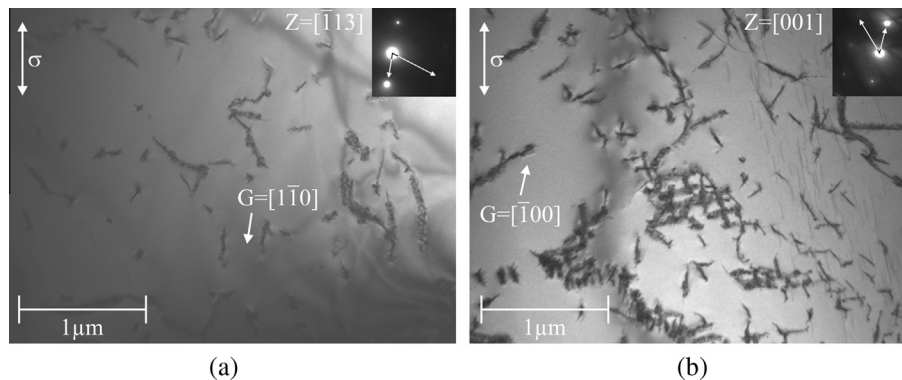


Fig. 11. TEM-micrographs of ferrite after a load-increase test finished at 300 MPa with precipitates (a) and precipitates with additional dislocations (b).

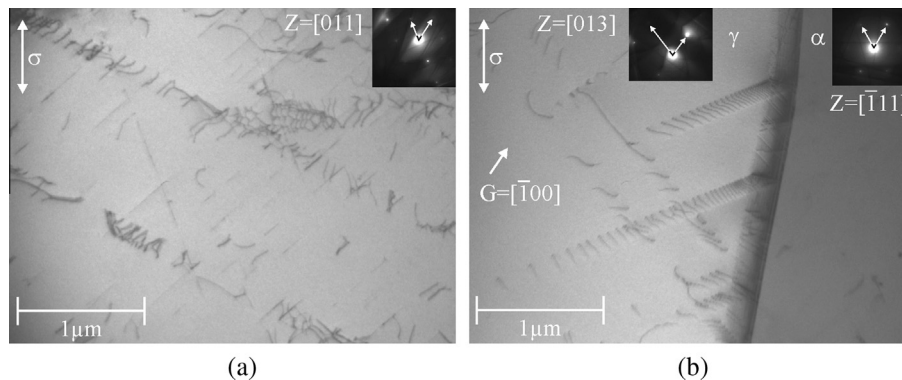


Fig. 12. TEM-micrographs of austenite (a) and an α/γ -phase boundary (b) from a LIT finished at 300 MPa.

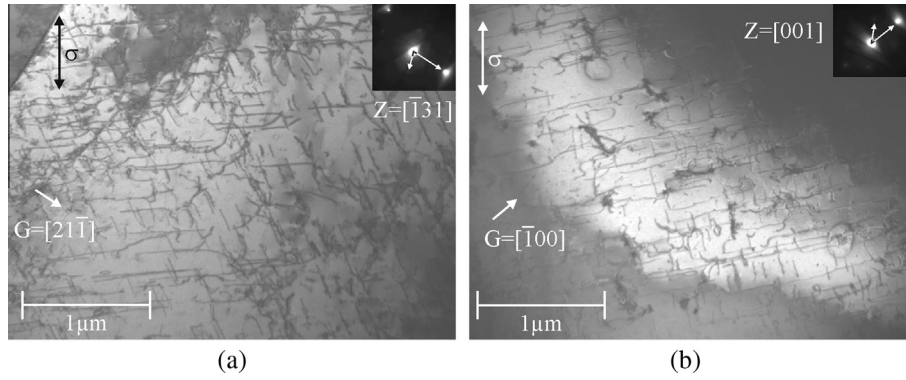


Fig. 13. TEM-micrographs of two ferrite grains (a)+(b) of a sample after a LIT finished at 380 MPa.

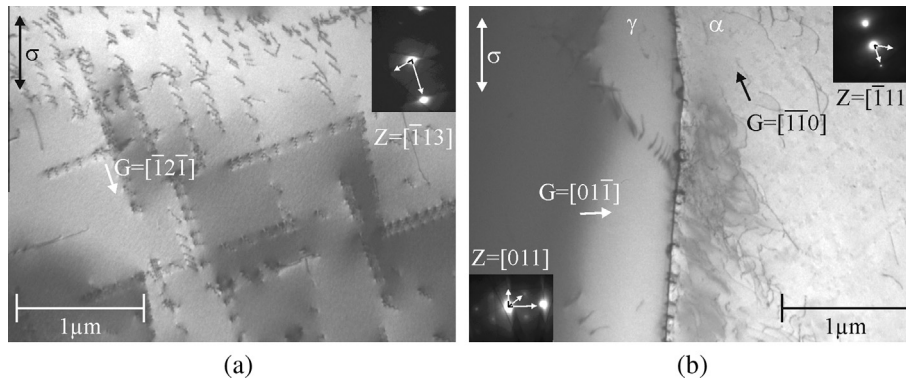


Fig. 14. TEM-micrographs of austenite (a) and an α/γ -phase boundary (b) of a sample after a LIT finished at 380 MPa.

Additionally, the TEM investigation proved that the material investigated does not show severe discontinuous changes in the microstructure, like local phase transformations. A limitation of “PHYBAL_{LIT}” may be that a distinct transient behaviour on the scale of only a few grains which may be very sensitive to the applied stress amplitude would not be visible in the $\varepsilon_{a,p}$, ΔT - and ΔR -signals. But all in all, it can be stated that the microstructural findings are in excellent correspondence with the macroscopic findings on the cyclic stress–strain behaviour and the monitored integral quantities $\varepsilon_{a,p}$, ΔT and ΔR .

4.4. Physically based fatigue life calculation method “PHYBAL_{LIT}”

The physically based fatigue life calculation method “PHYBAL_{LIT}” allows the calculation of Woehler (S–N) curves of metallic materials on the basis of generalized Morrow [24] and Basquin [25] equations with data from only one LIT and two CATs. This time-saving procedure is explained in detail in [18,19]. In addition to the one LIT shown in Fig. 6, the two CATs were performed at the stress amplitudes of 400 MPa and 420 MPa, respectively. These stress amplitudes were chosen such as to lie above the estimated endurance limit and below the stress amplitude leading to failure in the LIT. The cyclic deformation curves at a frequency of 5 Hz are given in Fig. 15 in terms of the change in temperature and electrical resistance.

For total strain controlled fatigue tests, cyclic deformation curves for the investigated material are shown in [26]. For lifetimes $>10^5$ cycles, the change in temperature decreases due to heat transfer saturation effects while the electrical resistance shows the cumulative fatigue damage with continuously increasing values.

The used measures are integral values representing fatigue induced microstructural changes e.g. dislocation reactions as well as micro-/macrocrack formation and propagation. Contrary to other methods related to individual material mechanisms e.g. growing short cracks [27], the “PHYBAL_{LIT}” method is based on the integral information of the material response. In Fig. 16, the cyclic stress–electrical resistance (CSR) curve of the LIT is shown for ΔR values, which are average values from each stress amplitude in the range of $390 \text{ MPa} \leq \sigma_a \leq 430 \text{ MPa}$. Furthermore, for both CATs represented in Fig. 15 the ΔR values at 10^4 cycles are used. At first, the ratio $Q(\sigma_a)_{\Delta R}$ was determined by dividing the ΔR value of each of both CATs by the corresponding average ΔR value

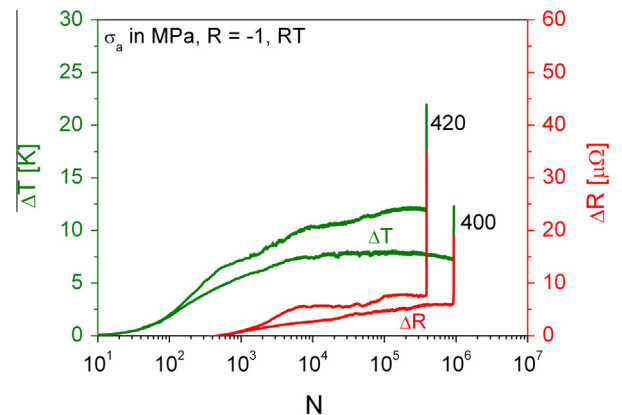


Fig. 15. Cyclic deformation curves showing the change in temperature ΔT and electrical resistance ΔR in two CATs carried out at 400 MPa and 420 MPa, respectively.

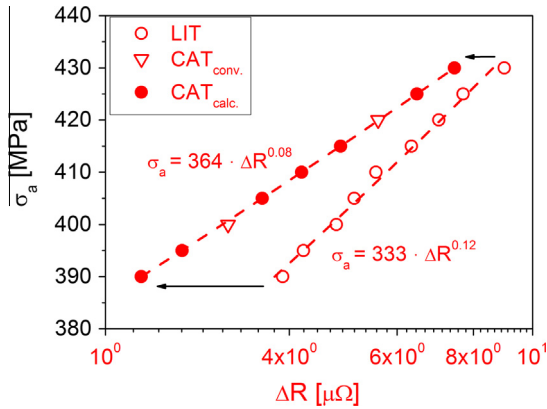


Fig. 16. Calculation of the cyclic stress–electrical resistance curve for constant amplitude loading.

measured in the LIT at the same stress amplitude. For all other stress amplitudes $Q(\sigma_a)_{\Delta R}$ was calculated by linear interpolation or extrapolation using the two values determined as described above as reference points. Then, the new CSR curve for constant amplitude loading was calculated by multiplying all ΔR values of the LIT with the appropriate ratio $Q(\sigma_a)_{\Delta R}$. This procedure can be performed accordingly using $\varepsilon_{a,p}$, ΔT or Δf as parameter instead of ΔR as shown for different steels and lightweight materials in [18,19]. In the next step of the “PHYBAL_{LIT}” calculation, the thus obtained CSR curve for constant amplitude loading is transformed into an S – N curve applying the well-known approximation of Morrow [24] by means of which the cyclic strength coefficient of the S – N curve can be derived from the cyclic hardening exponent of the CSR curve. Based on the cyclic hardening exponent $n'_{\Delta R}$ of 0.08 and the lifetime observed in the CAT at $\sigma_a = 420$ MPa the fatigue life calculation can be performed.

In Fig. 17, the S – N curves calculated by “PHYBAL_{LIT}” on the basis of the plastic strain amplitude $\varepsilon_{a,p}$, the change in temperature ΔT and the electrical resistance ΔR taken at 10^4 cycles are shown. Due to the high degree of energy dissipation in the investigated duplex steel, the change in temperature shows a more conservative result as compared to the plastic strain amplitude and the change in electrical resistance.

The calculated S – N curves lie within the scatter of the conventionally determined ones for $f = 5, 15, 130$ and 300 Hz. Fig. 18 exemplarily shows the “PHYBAL_{LIT}”-curve for the calculation on the basis of the change in electrical resistance. The lifetimes calculated on the basis of “PHYBAL_{LIT}” result in an excellent accordance

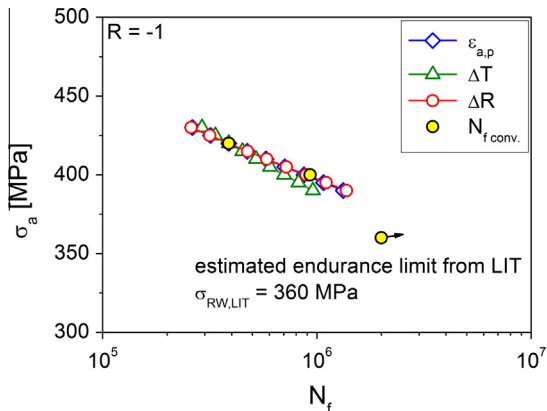


Fig. 17. Conventionally determined lifetimes $N_{f \text{ conv.}}$ compared to the predicted S – N curves based on “PHYBAL_{LIT}”.

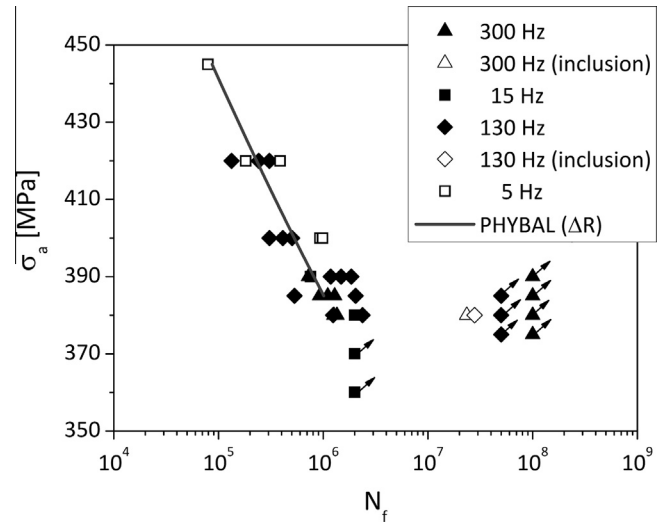


Fig. 18. Conventionally determined lifetimes for all frequencies compared to the calculated “PHYBAL_{LIT}”-curve on the base of the change in electrical resistance.

to the conventionally determined ones. To take the influence of the different testing systems and frequencies into account the average lifetimes of the constant amplitude tests at $\sigma_a = 420$ MPa are used for the “PHYBAL_{LIT}” calculation in this case.

For the conventional procedure to evaluate fatigue data, the lifetimes within the HCF regime were not statistically validated within this work. Moreover, the fatigue strength of $\sigma_a = 382$ MPa for a maximum number of 10^8 cycles was determined by the stair-case method.

5. Conclusions

The fatigue behaviour of the duplex stainless steel AISI 329 LN was investigated and the macroscopic observations obtained in fatigue tests were correlated with the results of detailed TEM investigations. The fatigue lifetime calculation method “PHYBAL_{LIT}” was applied using few selected fatigue results and compared to the conventionally obtained fatigue life data. It was shown that the parameters plastic strain amplitude, temperature, electrical resistance and resonant frequency can be equivalently used to characterise the fatigue behaviour of the investigated duplex steel in load increase (LITs) and constant amplitude tests (CATs) and for a reliable fatigue life assessment applying the “PHYBAL_{LIT}” method. The investigations were performed on four different testing systems with different test setups and frequencies.

The following conclusions can be drawn from the presented results:

- The different test setups, command signal shape and frequencies applied were found to have a minor effect on the S – N data, which were not statistically validated within this work.
- At low stress amplitudes mainly the softer austenite accommodates the plastic deformation. Although the material is deformed plastically, the strong barrier effect of the phase boundaries prevents the material from failure.
- At higher stress amplitudes dislocations can overcome the phase boundaries and allow cracks to initiate and grow resulting in final failure. The fatigue limit is thus defined by the strength of the phase boundaries.
- Load increase tests can be used for an assessment of the endurance limit.

- “PHYBAL_{LIT}” is a very powerful fatigue lifetime calculation method suitable for a fast calculation of *S–N* curves requiring only three fatigue tests.
- The average “PHYBAL_{LIT}”-curve based on data of the mechanical stress–strain hysteresis, temperature and electrical resistance measurements exhibits a very reasonable agreement to the conventionally determined data.
- Contrary to other methods in which the fatigue life is calculated on the basis of e.g. short crack growth, the “PHYBAL_{LIT}” method uses the integral information of the material response.
- An excellent correlation is also found between the macroscopically observed cyclic deformation behaviour and the TEM microstructural analysis.

Acknowledgements

The TEM investigation was supported by Agencia Nacional para la Promoción de la Ciencia, Técnica and Consejo Nacional de Investigaciones Científicas y Técnicas (CONICET) and by the cooperation program DAAD/MinCyT between Germany and Argentina.

References

- [1] Landgraf RW, Morrow J, Endo T. Determination of the cyclic stress–strain curve. *J Mater* 1969;4(1):176–88.
- [2] Lukáš P, Klesnil M. Cyclic stress–strain response and fatigue life of metals in low amplitude region. *Mater Sci Eng* 1973;11:345–56.
- [3] Dengel D, Harig H. Estimation of the fatigue limit by progressively-increasing load tests. *Fatigue Fract Eng Mater Struct* 1980;3:113–28.
- [4] La Rosa G, Risitano A. Thermographic methodology for rapid determination of the fatigue limit of materials and mechanical components. *Int J Fatigue* 2000;22(1):65–73.
- [5] Fargione G, Geraci A, La Rosa G, Risitano A. Rapid determination of the fatigue curve by the thermographic method. *Int J Fatigue* 2002;24(1):11–9.
- [6] Curà F, Curti G, Sesana R. A new iteration method for the thermographic determination of fatigue limit in steels. *Int J Fatigue* 2005;27(4):453–9.
- [7] Meneghetti G. Analysis of the fatigue strength of a stainless steel based on the energy dissipation. *Int J Fatigue* 2007;29(1):81–94.
- [8] Pandey KN, Chand S. Analysis of temperature distribution near the crack tip under constant amplitude loading. *Fatigue Fract Eng Mater Struct* 2008;31(5):316–26.
- [9] Polák J. Electrical resistivity of cyclically deformed copper. *Czech J Phys B* 1969;19(3):315–22.
- [10] Charrier J, Roux R. Evolution of damage fatigue by electrical measure on smooth cylindrical specimens. *Nondestruct Test Eval* 1991;6:113–24.
- [11] Constable JH, Sahay C. Electrical resistance as an indicator of fatigue. *IEEE T Compon Hybr* 1992;15(6):1138–45.
- [12] Chung DDL. Structural health monitoring by electrical resistance measurement. *Smart Mater Struct* 2001;10:624–36.
- [13] Sun B, Yang L, Guo Y. A high-cycle fatigue accumulation model based on electrical resistance for structural steels. *Fatigue Fract Eng Mater Struct* 2007;30(11):1052–62.
- [14] Mughrabi H. Specific features and mechanisms of fatigue in the ultrahigh-cycle regime. *Int J Fatigue* 2006;28(11):1501.
- [15] Strubbia R, Hereñú S, Marinelli MC, Alvarez-Armas I. Short crack nucleation and growth in lean duplex stainless steels fatigued at room temperature. *Int J Fatigue* 2012;41:90.
- [16] Mateo A, Gironès A, Keichel J, Llanes L, Akdut N, Anglada M. Cyclic deformation behavior of super duplex stainless steels. *Mater Sci Eng, A* 2001;314:176.
- [17] Souza MCL, Gomes de Abreu HF, Tavares SSM, da Fonseca Costa Filho MA. Effect of Mo concentration and aging time on the magnetic and mechanical hardness of Fe-xMo-5Ni-0.05C alloys. *Mater Res* 2009;12(4):423.
- [18] Starke P, Walther F, Eifler D. Fatigue life calculation of quenched and tempered steel SAE 4140 based on stress–strain hysteresis, temperature and electrical resistance measurements. *Fatigue Fract Eng Mater Struct* 2007;30(11):1044–51.
- [19] Starke P, Walther F, Eifler D. PHYBAL – a new method for lifetime prediction based on strain, temperature and electrical measurements. *Int J Fatigue* 2006;28(9):1028–36.
- [20] Nilsson JO. Super duplex stainless steel. *Mater Sci Technol* 1992;8:685–700.
- [21] Hertzman S, Charles J. On the effect of nitrogen on duplex stainless steels. *Revue de Metallurgie* 2011;108:413.
- [22] Akdut N. Phase morphology and fatigue lives of nitrogen alloyed duplex stainless steels. *Int J Fatigue* 1999;21:97.
- [23] Mughrabi H, Herz K, Stark X. Cyclic deformation and fatigue behaviour of α -iron mono- and polycrystals. *Int J Fract* 1981;17:193–220.
- [24] Morrow JD. Cyclic plastic strain energy and fatigue of metals. *ASTM-Internal Friction, Damping and Cyclic Plasticity STP* 1964;378:45–87.
- [25] Basquin OH. The exponential law on endurance tests. *Proc ASTM* 1910;10:625–30.
- [26] Sahu JK, Ghosh RN, Christ H-J. Low cycle fatigue behaviour of duplex stainless steel: influence of isothermal aging treatment. *Fatigue Fract Eng Mater Struct* 2009;33:77–86.
- [27] Goto M, Nisitani H. Fatigue life prediction of heat-treated carbon steels and low alloy steels based on a small crack growth law. *Fatigue Fract Eng Mater Struct* 1994;17:171–85.